Diffusion and electrical conductivity in water at ultrahigh pressures

Martin French,[1] Thomas R. Mattsson,[2] and Ronald Redmer[1]

[1]*Institut für Physik, Universität Rostock, D-18051 Rostock, Germany*

[2]*HEDP Theory, MS 1189, Sandia National Laboratories, Albuquerque, New Mexico 87185-1189, USA*

We calculate the electrical conductivity of water for ultrahigh pressures up to 80 Mbar and temperatures up to 130 000 K as relevant for planetary physics by using *ab initio* molecular-dynamics simulations. The electron system is treated within density-functional theory and the electronic conductivity is obtained from an evaluation of the Kubo-Greenwood formula. The ionic conductivity is determined via diffusion coefficients. Our calculations reproduce most of the available experimental conductivity data within the error bars while the conductivity plateau measured by Mitchell and Nellis cannot be reproduced. At high densities a pressure-induced nonmetal-to-metal transition is predicted within the superionic phase. Furthermore, we study the influence of exchange and correlations on the electronic conductivity in more detail by applying a standard generalized gradient approximation and a hybrid functional as well that includes screened Fock exchange. The latter treatment yields a larger band gap and thus more reliable electrical conductivities, especially in the region of the nonmetal-to-metal transition. These results are relevant as input for future interior and dynamo models of giant, water-rich planets.

I. INTRODUCTION

Charge transport in water at ambient conditions qualitatively operates via protons hopping from H_3O^+ ions to H_2O molecules (or analogous from H_2O molecules to OH^- ions) along hydrogen-bonded chains, the well-known Grotthuss mechanism.[1] Quantitatively, the conductivity has been measured with high accuracy for pressures up to 100 kbar and temperatures up to 1000 °C.[2] Measurements for higher pressures and temperatures were performed with shock-wave experiments[3–6] which usually have larger error bars. The conductivity increases strongly with pressure and temperature up to values of about $200/\Omega$ cm.[5,6] Protons are still the dominant charge carriers in this domain which stem from dissociation of water molecules.[7,8] *Ab initio* computer simulations have predicted that water is fully dissociated above 5000 K (Refs. 9 and 10) in the fluid phase, and that a *superionic* phase occurs at high pressures.[11–15] This exotic phase consists of a solid bcc oxygen lattice while the protons are mobile and enable a high electrical conductivity. The measurement of a new triple point along the ice VII melting curve probably marks the transition to superionic water although this issue is still under discussion.[14,16–20]

In addition to the protonic conductivity, also electronic conductivity emerges at high pressures, as reflectivity measurements up to several megabar along Hugoniot curves[21,22] indicate. Theoretical approaches[9,13] were developed to treat the effects of dissociation and ionization on the conductivity of water. These results show signs of a complex behavior of the electronic conductivity that becomes relevant above 4000 K in the fluid phase but that is suppressed in the superionic phase.

In this paper, we apply *ab initio* molecular-dynamics (MD) simulations in order to calculate diffusion coefficients and electrical conductivity data up to extreme pressures of 80 Mbar and temperatures of 130 000 K. This method includes a quantum-statistical treatment of the electron system by us-ing finite-temperature density-functional theory (FT-DFT) that takes into account thermal excitations of the electrons. Such an approach has been successful in treating matter under extreme conditions such as shocked deuterium[23] and carbon[24] with high accuracy. Recently, the method was used to study properties of shocked hydrocarbon polymers,[25] demonstrating its applicability also to complex materials.

We have applied this method to calculate the equation of state (EOS) data and the phase diagram of water up to such ultrahigh pressures[15] which are not yet accessible with current dynamic compression techniques but are nevertheless relevant for astrophysics.[26,27] This EOS data as well as the electrical conductivity are of paramount importance in order to model the interior[28–32] and the magnetic field structure[33,34] of giant planets, especially for Uranus and Neptune which probably contain large fractions of water. Recently we could show that the predictions of respective dynamo models[33,34] for both planets are in striking agreement with interior models[35] that are based on *ab initio* data.[15,36,37] Another interesting application of high-pressure water data is the modeling of water-rich extra-solar giant planets, such as GJ 436b,[38] which will also be detected within the CoRoT and Kepler missions. Finally, the cores of Jupiter and Saturn are expected to consist largely of heavier elements, among them water. To determine the thermodynamic state and its conductivity for such extreme conditions of several 10 Mbar and temperatures of several 10^3 K is a great challenge to high-pressure physics.

Our paper is organized as follows: details of the *ab initio* simulation technique are given in Sec. II. The ionic conductivity is derived from the ion diffusion coefficients via a generalized Einstein formula as outlined in Sec. III. Results for the electronic conductivity, which is obtained by evaluating the Kubo-Greenwood formula, are presented in Sec. IV. The total conductivity as well as a comparison with experimental data, is given in Sec. V, followed by conclusions. Good agreement of our *ab initio* results with available experimental conductivity data is found.

In our electronic conductivity calculations, we pay special attention to the band gap, that constitutes a fundamental challenge for density-functional theory because the gap is typically underestimated. This problem can be tackled, e.g., with hybrid functionals that contain nonlocal Fock exchange, like that from Heyd, Scuseria, and Ernzerhof (HSE).[39,40] We study the impact of the HSE functional on the electrical conductivity, especially in the superionic phase and in the region of the nonmetal-to-metal transition at ultrahigh pressures.

II. *AB INITIO* SIMULATIONS

Our electrical conductivity calculations are based on FT-DFT-MD simulations in the Born-Oppenheimer approximation which are performed with the Vienna *ab initio* simulation package (VASP) 4.6.28 and 5.2.2.[41–45] Hereby the ions are propagated via a classical molecular-dynamics algorithm by forces that are derived from the FT-DFT (Refs. [46–48]) treatment of the electron system at each time step. Periodic boundary conditions are employed and the electronic wave functions are expanded in a plane-wave basis set. Projector-augmented wave (PAW) potentials[44,49] provided with VASP are used for the electron-ion interaction. In all FT-DFT-MD simulations, the exchange-correlation functional is evaluated in the generalized gradient approximation of Perdew, Burke, and Ernzerhof (PBE).[50]

For the ionic conductivity we employ the model of Mattsson and Desjarlais[13] which requires the computation of the diffusion coefficients (obtained through the mean-square displacement method) of both ion species as well as the fraction of protons bound to oxygen ions. The present calculations generally use the same simulation parameters (54 molecules and the standard VASP PAW pseudopotentials which treat six electrons per oxygen ion and one per hydrogen self-consistently within the FT-DFT and a plane-wave cutoff of 900 eV) which have produced well-converged results in earlier simulations[13,15] (labeled there as quantum molecular dynamics instead of FT-DFT-MD).

The electronic conductivity is directly calculated from the FT-DFT eigenvalues and wave functions via the Kubo-Greenwood formula.[51,52] In many calculations we observed that it is necessary to employ an all electron PAW core potential for oxygen to obtain fully converged electronic conductivities throughout the density and temperature regime considered here. Extensive convergence tests with respect to **k**-point sampling and particle numbers are also made. In addition, several electronic conductivity calculations are carried out with the HSE hybrid functional[39,40] which yields larger electronic band gaps[53,54] compared with the PBE functional.

III. IONIC CONDUCTIVITY

A. Generalized Einstein formula

Under ambient conditions only 10^{-7} mol/l of charge carrying OH^- and H_3O^+ ions exist in water which cause an electrical conductivity[55] of $5.5 \times 10^{-7}/\Omega$ cm through protons diffusing via the Grotthuss mechanism.[1] At high pressures and temperatures, the lifetime of associated species such as H_2O, OH^-, and H_3O^+ is significantly reduced[7–9,12,13] which leads to an increased conductivity. Mattsson and Desjarlais[13] have proposed a model to calculate the proton conductivity from FT-DFT-MD simulations that accounts for the Grotthuss mechanism but that does not require a detailed analysis of the molecular and ionic aggregates involved. The respective expression

$$\sigma_p = \frac{e^2 n_p}{k_B T}(D_p - \gamma D_O),\tag{1}$$

is a generalized Einstein formula where $+e$ is the proton charge (see Appendix A for additional information), n_p is the number of protons per volume, and $k_B T$ is the thermal energy. D_p and D_O are the diffusion coefficients of protons and oxygen nuclei, and γ is the fraction of protons bound to O^{2-} ions. The minus sign in Eq. (1) arises from the formation of associated species from protons and O^{2-} ions which do not contribute to the conductivity. For instance, when all protons and oxygen ions form water molecules ($\gamma = 1$), both ion species have the same diffusion coefficients and no proton conductivity occurs. Dissociation is accompanied by a nonzero difference in the diffusion coefficients of both ion species and a reduction in γ. Equation (1) is also valid in the superionic phase where no oxygen diffusion takes place.

When the dissociation of water molecules is strong, mobile oxygen ions also add to the ionic conductivity similar as in a molten salt. However, their contribution is negligible compared to the proton conductivity and will not be considered any further, see Appendix B for details.

B. Ion diffusion coefficients

The ion diffusion coefficients are calculated from FT-DFT-MD simulation runs in the canonical ensemble where the temperature is controlled by a Nosé thermostat[56] for temperatures between 1000 and 24 000 K and densities ranging from 1 up to 13 g/cm^3. Additional simulations with temperatures up to 130 000 K were run within a narrow density regime between 3 and 4 g/cm^3, which corresponds to states along the principal Hugoniot curve. Equilibrated simulation runs which have served to calculate EOS data before[15] were continued for additional 4–8 ps. Then the diffusion coefficients of both ion species were calculated via the mean-square displacement method. Several other simulation runs were performed in the microcanonical ensemble to check if the Nosé thermostat has an influence on the diffusion coefficients, this was not the case. The simulation boxes contained 54 oxygen ions and 108 protons in most cases. For temperatures higher than 50 000 K we used 16 oxygen ions and 32 protons, respectively. The time steps varied between 0.2 and 0.5 fs depending on the location in the density-temperature plane. The standard PAW potentials from VASP together with a plane-wave cutoff of 900 eV were used and the electronic wave functions were calculated at the Γ point. We have shown earlier that these parameters produce well-converged simulations runs.[13,15]

The proton diffusion coefficient is displayed in Fig. 1. It increases with the temperature and decreases with the density. Surprisingly, there is no sign that the phase transition
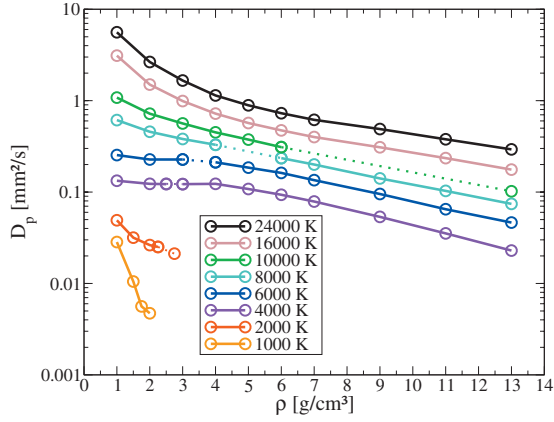
FIG. 1. (Color) Proton diffusion coefficient up to 13 g/cm^3. The dotted lines indicate the location of the phase transition between the plasma and the superionic phase (Ref. 15).

between the fluid and the superionic phase influences the proton diffusion coefficient. We believe that the reason for this smooth behavior is that the large vibrational amplitude of the oxygen ions on their lattice sites creates oxygen ion configurations of low symmetry, similar to a fluid, for the short times that protons need to pass. We estimate the statistical error in the proton diffusion coefficient to be less than 10%.

The oxygen diffusion coefficient also shows a systematic increase with the temperature as well as a decrease with the density until it vanishes in the superionic phase. It is lower than the proton diffusion coefficient for all parameters considered here. The statistical error is estimated to be less than 20%, Fig. 2.

C. Fraction of protons bound to oxygens

The number of protons bound to oxygen ions can be estimated easily in the largely molecular regime for temperatures below about 2000 K. By matching each proton to its nearest oxygen neighbor[8] one obtains a distribution of oxygen ions with one, two, or three protons associated with it which can be identified as OH$^-$, H$_2$O, and H$_3$O$^+$ (although not carried out in this work, the charges can be deduced, e.g.,
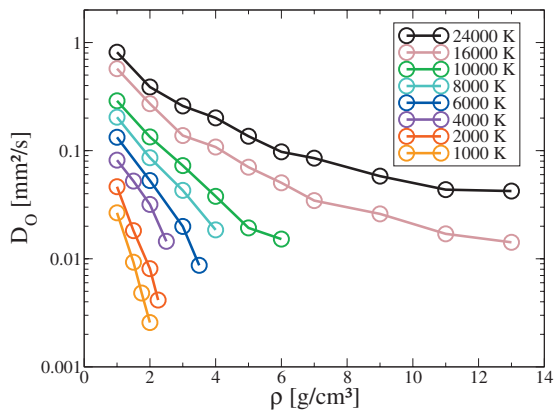
FIG. 2. (Color) Oxygen diffusion coefficient up to 13 g/cm^3 in the fluid phase.
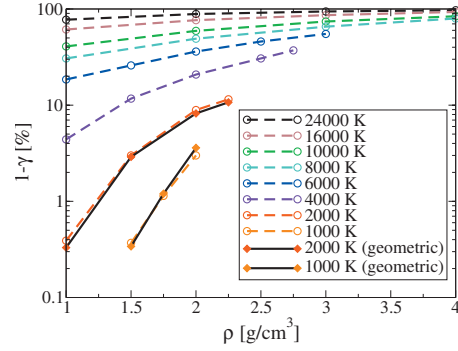
FIG. 3. (Color) Fraction of protons which participate in charge transport in fluid water. The solid lines result from the geometric approach while the dashed lines are obtained with the procedure described in the text with $\Delta t = 5$ fs.

from a Wannier center analysis[8,13] but not from sole geometric ion arrangements). There is one OH$^-$ ion for each H$_3$O$^+$ ion which is consistent with global charge neutrality. The present calculations reproduce the earlier findings of Schwegler *et al.*[8] well. For each OH$^-$ or H$_3$O$^+$ ion one proton can contribute to the conductivity via the Grotthuss mechanism, all other protons are bound. The fraction of bound protons is therefore $\gamma = 1 - (N_{OH^-} + N_{H_3O^+})/N_{p,total}$, where N_i are the particle numbers of the respective species.

However, such a simple geometric approach is not applicable at higher temperatures where more and more protons become free until all molecules are completely dissociated. At that point, also mobile protons which happen to pass close to a particular oxygen ion are counted as bound to it. As a consequence, in hot disordered systems this method becomes unreliable as it reports oxygen ions having zero or more than three associated protons.

A possible solution to this problem is to define a critical radius r_c around an oxygen ion in which a proton has to stay for a certain time interval t_c to be counted as bound.[9,12,13] However, this procedure introduces two free parameters (radius r_c and time interval t_c) which have to be chosen by intuition and on which the results depend.

Here we use an alternative procedure which inverts the
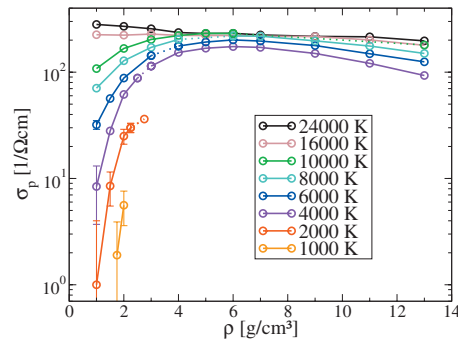
FIG. 4. (Color) Proton conductivity up to 15 g/cm^3. The dotted lines indicate the location of the phase transition between the plasma and the superionic phase (Ref. 15). The 1000 and 2000 K lines end as soon as the insulating ice phases occur at higher densities.

problem and estimates the fraction of *unbound* protons instead. For each proton we determine its nearest oxygen neighbor at every time step. We assume that a proton which changes its nearest oxygen neighbor is, for a certain time, in an unbound state. Thus we attribute each proton as unbound for a defined time interval Δt before and after all events that change its oxygen neighbor during the simulation. Summing up the whole time that a proton is attributed unbound divided by the total simulation time and averaging over all protons gives the fraction of unbound protons $1 - \gamma$. The time interval Δt is a parameter which we fit in such a manner that the results are concordant with those obtained by the geometric method (that was also used by Schwegler *et al.*[8]) at 1000 and 2000 K, which we find to work reliable in that regime. A value of $\Delta t = 5$ fs yields the best coincidence. The fraction of unbound protons is displayed in Fig. 3 for the fluid phase. It increases systematically with temperature and density. In the superionic phase the fraction of bound protons has no influence on the conductivity, see Eq. (1), because the oxygen ions are immobile ($D_O = 0$). Although not shown in Fig. 3, the number of bound protons decreases to zero at higher densities.

D. Protonic conductivity results

The protonic conductivity, shown in Fig. 4, increases strongly with the temperature until it levels off at about $200/\Omega$ cm. This behavior is caused by dissociation of water molecules which lead to increased amounts of charge carriers. The strong rise of the proton conductivity with the density is also due to dissociation. At higher densities where water is strongly dissociated or superionic, the maximum and the subsequent decrease in the conductivity is produced by increasing proton densities and decreasing diffusion coefficients which partially compensate each other, see Eq. (1). There is no sign of a discontinuity at the phase boundary between the fluid and the superionic phase. The uncertainty in the conductivity data stems mainly from the proton diffusion coefficient and amounts up to approximately 10% in general. This error is larger especially for lower conductivity values because of the small concentration of dissociated molecules in a simulation box containing about 100 particles. Therefore, the difference between the diffusion coefficients in Eq. (1) becomes small. To calculate proton conductivities below $1/\Omega$ cm with this method, simulations with substantially greater particle numbers have to be performed which is beyond the computational capacity currently available. The protonic conductivities reported here are in good agreement with earlier calculations that reached up to 3 g/cm^3 and 6000 K.[11,13]

IV. ELECTRONIC CONDUCTIVITY

A. Kubo-Greenwood formula

The real part of the electronic conductivity is calculated via the Kubo-Greenwood formula[51,52]

$$\sigma_e(\omega) = \frac{2\pi e^2}{3m^2\omega V} \sum_{\mathbf{k}} w_{\mathbf{k}} \sum_{j=1}^{N_b} \sum_{i=1}^{N_b} \sum_{\alpha=1}^{3} [f(\epsilon_{j,\mathbf{k}}) - f(\epsilon_{i,\mathbf{k}})]$$
$$\times |\langle \Psi_{j,\mathbf{k}} | \hat{p}_\alpha | \Psi_{i,\mathbf{k}} \rangle|^2 \delta(\epsilon_{i,\mathbf{k}} - \epsilon_{j,\mathbf{k}} - \hbar\omega), \quad (2)$$

where m is the electron mass, V the volume of the cubic

simulation cell, and ω the frequency. The indices i and j run over all N_b bands and sum the matrix elements[57] of the Bloch functions with the momentum operator weighted by the difference of the Fermi occupations $f(\epsilon_{i,\mathbf{k}})$ of the bands. The α sum averages over the three spatial directions. The integration over the first Brillouin zone is evaluated with a discrete mesh of $\mathbf{k}$ points and their respective weights $w_{\mathbf{k}}$. Since all bands have discrete eigenvalues, the δ function has to be broadened to a finite width; a Gaussian shape has proven to be convenient.[58] Then the limit $\omega \to 0$ is taken because only the static (dc) part is of interest here. For each point in the temperature and density plane, Eq. (2) is applied on FT-DFT eigenvalues and eigenfunctions obtained from 10–30 different ion configurations. The respective results are then averaged. The ion configurations were taken from converged simulation runs in thermodynamic equilibrium.[15] Most of these calculations were performed with 54 oxygen and 108 hydrogen ions, i.e., 54 molecules in the simulation box. Only for the highest temperatures $T \geq 50\,000$ K we have used smaller particle numbers (16 oxygen and 32 hydrogen ions), i.e., 16 molecules in the box. Convergence tests were also done with higher particle numbers. The electronic conductivity calculations were carried out with an all electron PAW core potential (converged conductivities are obtained with an 800 eV cutoff) for oxygen because the standard six electron potential yielded up to 25% lower conductivities, especially in the high-density regime. However, no thermal excitations of the deeply bound (several 100 eV) 1s oxygen electrons were observed.

B. Calculations with the PBE functional

First we evaluate the Kubo-Greenwood Eq. (2) with eigenvalues and eigenfunctions calculated with the PBE functional. Several convergence tests regarding the number of $\mathbf{k}$ points are carried out. In the fluid phase, the mean value point (MVP) (Ref. 59) yields well-converged results. A $4 \times 4 \times 4$ mesh[60] is employed in the superionic phase although the results with the MVP are already feasible there. Tables I and II contain results of convergence tests with respect to the number of $\mathbf{k}$ points and the particle number. The required number of $\mathbf{k}$ points increases with the density, especially in the superionic phase. We attribute this effect to both a transition to metallic behavior and to a more pronounced influence of the band dispersion because of the larger first Brillouin zones. Calculations with higher particle numbers generally require fewer $\mathbf{k}$ points to converge.

The results for the electronic conductivity calculated with the PBE functional are displayed in Fig. 5. In the fluid phase the conductivity increases with density and temperature which is due to ionization processes. Interestingly, the transition to the superionic phase is accompanied by a reduction in the electron density of states near the chemical potential of the electrons (Fermi energy). This leads to a drop in the conductivity as was already found by Mattsson and Desjarlais.[13] This effect is particularly strong at 4000 K but less pronounced at higher temperatures because of thermal activation of electrons. With increasing density our calculations predict a strong increase of the conductivity in the su-

TABLE I. Comparison of the electronic conductivities calculated with the PBE functional and different **k**-point samplings at several densities and temperatures in the fluid phase. N is the number of molecules.

T (K)	ϱ (g/cm^3)	N	**k** points	σ_e (1/Ω cm)
8000	3	54	Γ	980 ± 100
8000	3	54	MVP	970 ± 110
8000	3	54	$3\times3\times3$	1000 ± 100
8000	3	128	MVP	1010 ± 90
24000	1	54	Γ	530 ± 40
24000	1	54	MVP	510 ± 40
24000	1	54	$3\times3\times3$	500 ± 40
24000	5	54	Γ	4700 ± 400
24000	5	54	MVP	4700 ± 300
24000	5	54	$3\times3\times3$	4700 ± 300
24000	5	128	MVP	4800 ± 300
24000	15	54	Γ	14500 ± 900
24000	15	54	MVP	12800 ± 700
24000	15	54	$3\times3\times3$	13000 ± 800
24000	15	54	$4\times4\times4$	13000 ± 700
100000	3.5	16	Γ	4440 ± 150
100000	3.5	16	MVP	4270 ± 120
100000	3.5	16	$3\times3\times3$	4150 ± 100
100000	3.5	27	MVP	4000 ± 200

TABLE II. Comparison of the electronic conductivities calculated with the PBE functional and different **k**-point samplings at several densities and temperatures in the superionic phase. N is the number of molecules.

T (K)	ϱ (g/cm^3)	N	**k** points	σ_e (1/Ω cm)
4000	3	54	Γ	5.3 ± 1.3
4000	3	54	MVP	7.3 ± 1.7
4000	3	54	$3\times3\times3$	6.9 ± 1.3
4000	3	54	$4\times4\times4$	6.8 ± 1.2
6000	5	54	Γ	110 ± 20
6000	5	54	MVP	200 ± 30
6000	5	54	$3\times3\times3$	210 ± 30
6000	5	54	$4\times4\times4$	220 ± 30
6000	5	128	MVP	210 ± 40
6000	5	128	$3\times3\times3$	220 ± 30
6000	13	54	Γ	3500 ± 400
6000	13	54	MVP	7700 ± 600
6000	13	54	$3\times3\times3$	9700 ± 800
6000	13	54	$4\times4\times4$	9700 ± 800
6000	13	128	MVP	7200 ± 700
6000	13	128	$3\times3\times3$	9600 ± 700
8000	9	54	Γ	970 ± 80
8000	9	54	MVP	5100 ± 500
8000	9	54	$3\times3\times3$	4300 ± 300
8000	9	54	$4\times4\times4$	4400 ± 300

perionic phase again and, eventually, a change from semiconducting (σ_e increases with T) to metallic (σ_e decreases with T) behavior. This *nonmetal-to-metal* transition occurs simultaneously with the proton rearrangement as observed earlier in that region.[15] The protons occupy ice X sites more frequently at lower densities but reside more often at octahedral sites in the high-density regime.

C. Calculations with the HSE functional

It is known that the PBE functional underestimates the electronic band gap in most systems. In order to tackle this problem, we apply the HSE hybrid functional[39,40] when calculating the Kohn-Sham eigenvalue spectrum. It replaces 1/4 of the DFT exchange with screened Fock exchange (screening parameter here: $\mu = 0.2$ Å^{-1}) and yields larger band gaps than PBE. These are well in line with experiments for many substances.[53,61] All HSE calculations were performed with VASP 5.2.2.

Since the overall performance of the MVP (Ref. [59]) in the PBE calculations is serviceable to excellent, we restricted all HSE calculations (which are about 100 times more expensive than PBE calculations) to that special **k** point. We compared the conductivities calculated with both the HSE and PBE functional at the MVP for several ion configurations (three in the fluid and ten in the superionic phase) for each density and temperature and derived a correction factor. In general, the HSE functional shifts electronic states below the chemical potential of the electrons to lower energies and

states above the chemical potential to higher energies. When the band gap is closed the HSE functional reduces the density of states near the chemical potential compared with the PBE values. Therefore, the HSE conductivities are always smaller than the PBE conductivities but the difference decreases at the highest temperatures. For instance, at 130 000 K the correction factor is only $\sigma_{\text{HSE}}/\sigma_{\text{PBE}} = 0.9$. Figure 6 shows the correction factor for temperatures up to 24 000 K. In the fluid phase we find a temperature-dependent factor of 0.5–0.7 which applies in the whole density range. In the low density, semiconducting superionic phase the HSE conductivities are up to one magnitude lower than the PBE values, i.e., the discontinuity of the electronic conductivity from the fluid to the superionic phase becomes more pronounced. This indicates clearly that electrons are more strongly bound in the low-density superionic phase. As soon as superionic water shows metallic behavior at higher densities the difference between the HSE and the PBE conductivities becomes smaller and reaches numbers that are roughly comparable with those found in the fluid phase. Furthermore, the conductivity isotherms in the very dense superionic phase gradually approach each other without significant crossings.

V. RESULTS

A. Total electrical conductivity

The total conductivity consisting of the protonic and electronic conductivity (the latter including the correction factor
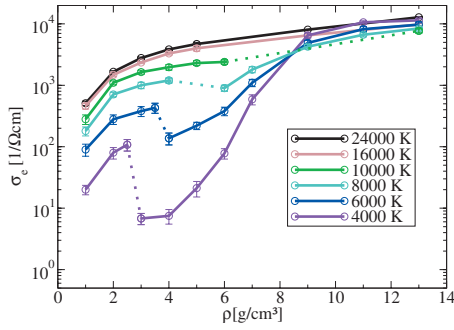
FIG. 5. (Color) Electronic conductivity calculated with the PBE functional. The dotted lines indicate the location of the phase transition between the plasma and the superionic phase (Ref. 15) which is accompanied by a discontinuity in the conductivity. Error bars are from statistical averages over 10–30 ion configurations.

from the HSE functional) is plotted in Fig. 7. The error bars in the very dense superionic phase were estimated to be approximately 30%, mainly because the determination of the correction factor was based only on the MVP. The sharp discontinuity in the electronic conductivity at the transition from the fluid to the superionic phase is diminished by the smooth protonic contribution. The total conductivity therefore drops only by a factor of about two between 4000 and 8000 K crossing the phase transition line. Nevertheless, this discontinuity could be used to determine the transition to the superionic phase in future shock-wave experiments. In the fluid phase below 4000 K, the conductivity is mostly due to protons while the electronic contribution dominates at higher temperatures.

B. Electrical conductivity along the principal Hugoniot curve

The measurements of Hamann and Linton[3] along the principal Hugoniot curve of water show a strong increase in the electrical conductivity over several orders of magnitude. The experiments of Mitchell and Nellis[4] indicate that this strong
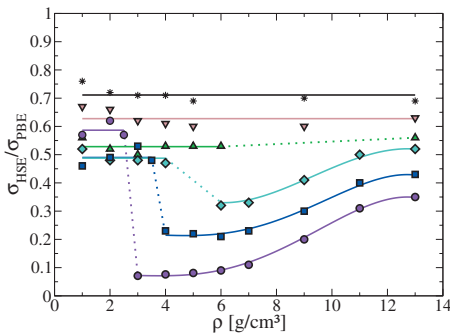
FIG. 6. (Color) Relation between the conductivities calculated with the PBE and the HSE functional at the MVP. The dotted lines indicate the location of the phase transition between the plasma and the superionic phase. The solid lines are fit curves. The colored symbols represent the following temperatures: black stars 24 000 K, brown downward triangles 16 000 K, green upward triangles 10 000 K, cyan diamonds 8000 K, blue squares 6000 K, and purple circles 4000 K.

increase levels off above 30 GPa at values of about $20/\Omega$ cm, see Fig. 8. In an earlier work, we have used our *ab initio* EOS data to calculate the Hugoniot curve which agrees with the experimental pressures, densities, and temperatures very well.[10] Figure 8 shows the total conductivities as calculated with the method described here along the Hugoniot curve in comparison with the experimental data mentioned above. While our results agree with the lower pressure data[3] very well, we see no indication of a flattening as found by Mitchell and Nellis.[4] Our simulations show that only 10% of the protons participate in the electrical conduction at 30 GPa (see Fig. 3), which was also observed by Goldman *et al.*[9] in their simulations. This explains why the theoretical protonic conductivity continues to rise up to maximum values of $200-300/\Omega$ cm at yet higher pressures (green curve). Furthermore, our calculations predict that the electronic contribution to the total conductivity becomes dominant above 60 GPa.

We find no explanation for a plateaulike structure as Mitchell and Nellis[4] have observed at about 30–60 GPa: both contributions to the total conductivity are rising smoothly with the pressure in that region. The ionic conductivities given by Goldman *et al.*[9] (red curve) are lower than ours

FIG. 7. (Color) Total electrical conductivity (electronic contribution including the HSE correction factor) as function of the density for various temperatures. The dotted lines indicate the location of the phase transition between the plasma and the superionic phase (Ref. 15).
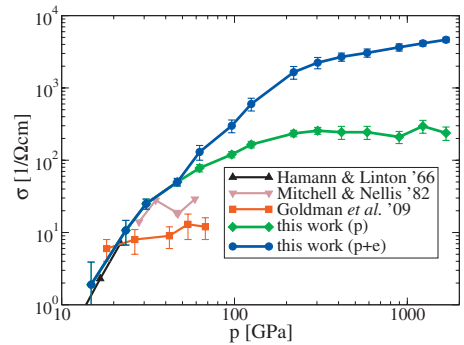
FIG. 8. (Color) Conductivity along the principal Hugoniot. Triangles and squares represent the experiments of Hamann and Linton (Ref. 3) and of Mitchell and Nellis (Ref. 4), respectively. The green curve is the protonic conductivity while the blue curve contains also the electronic contribution (including the HSE correction factor). The red squares are the values from Goldman *et al.* (Ref. 9).

TABLE III. Electrical conductivity σ_{exp} for thermodynamic states generated in shock-wave experiments (Ref. [6]) (temperatures taken from Ref. [21]) compared with the theoretical values σ_{th}. For simplicity we took averages over shots with very similar thermodynamic conditions as indicated. The experimental densities have error bars of about 10% and the temperatures of about 20%, respectively (Ref. [6]).

Shots	T (K)	ϱ (g/cm^3)	σ_{exp} (1/Ω cm)	σ_{th} (1/Ω cm)
11	1860	2.87	39 ± 12	6 ± 0.6
3	2550	3.08	109 ± 33	82 ± 9
4	3120	3.24	117 ± 35	95 ± 10
1,2,8,7	3820	3.36	151 ± 46	119 ± 12
5,9,10	5400	3.62	179 ± 54	185 ± 25

because they used an effective proton charge of $+0.37e$. We have also verified that conductivities derived from Eq. (1) show a much better convergence than those calculated via the full ionic current-current correlation function that Goldman *et al.*[9] have employed. The reason for this behavior is that Eq. (1) contains only diffusion coefficients (contributions of autocorrelations) which are not susceptible to the strong fluctuations that arise from the cross correlations of the protons in the full current-current-correlation function. Resolving the deviation between theory and experimental data near 50 GPa will require further experimental as well as theoretical efforts.

C. Comparison with reverberating shock-wave experiments

Reverberating shock waves yield an almost isentropic compression which allows to probe the temperature region below the principal Hugoniot where correlation effects are stronger. Conductivity measurements employing reverberating shock waves[5,6] found a saturation of the electrical conductivity between 100 and 200/Ω cm above 1 Mbar with only protons as charge carriers.[5] Inserting the densities given by Chau *et al.*[6] and the corrected temperatures reported later[21] into the phase diagram of water based on our recent *ab initio* EOS data,[15] one finds that the thermodynamic states achieved in these quasi-isentropic compression experiments are most probably located in the superionic phase.

We have performed additional calculations for the set of these experimental parameters and compare our results with the measured conductivities in Table III. The agreement is very good, except for the point with the lowest temperature which is very close to the phase transition line to ice VII. If the density and temperature is varied within the experimental error bars for that point, the calculated conductivity is also in accordance with the experimental value. We conclude that the theoretical conductivities are in very good agreement with results of reverberating shock-wave experiments.[5,6] Although they did not describe it as such, these experiments have most probably already probed the superionic water phase.

VI. CONCLUSIONS

We have calculated the ion diffusion coefficients and the electrical conductivity of water under extreme pressures with *ab initio* molecular-dynamics simulations. Both the protonic and electronic contributions are relevant and determined for a wide range of densities and temperatures. Our results are in good agreement with data from reverberating shock waves. We have no explanation for the plateaulike behavior as observed in Hugoniot experiments at 30–60 GPa but find a smooth increase in the conductivity instead. Most interestingly, our calculations predict a transition to metallic behavior within the superionic phase of water at high densities.

We examine the influence of the exchange-correlation functional (PBE vs the HSE hybrid functional) on the electronic conductivity. The respective correction factor is found to be only dependent on temperature in the fluid phase. In the superionic phase it rescales the electronic conductivity substantially by up to an order of magnitude. This finding is of general importance for electronic conductivity calculations using DFT methods. Our conductivity data can be applied to model planetary interiors and dynamos of water-rich giant planets such as Neptune and Uranus[35] or to locate the phase transition line between the fluid and the superionic phase via high-pressure experiments.

APPENDIX A: EFFECTIVE CHARGE TRANSPORTED BY PROTONS

The charge that the protons carry enters Eq. (1), and it is not trivial to show that the protons transport their elementary charge of $+e$ in water. Goldman *et al.*[9] employed the Mulliken charge method[62] that counts the population of electronic states around an ion and that leads to a screened proton charge of $+0.37e$ with small variations along the principal Hugoniot curve.[9] Also electron-proton pair-correlation functions show electron density centered around the protons, which delocalizes with increased density, see Fig. 9.

A different method for calculating ionic charges in nonmetallic systems is polarization theory[63–65] (also labeled as Berry phase technique) which determines the change in polarization when an ion is displaced a very small distance from its initial position. This allows one to derive the effective ionic charge by taking into account the screening of the electrons within a linear response framework. The application of this technique on our simulations yields an effective proton charge that varies barely with the temperature but that
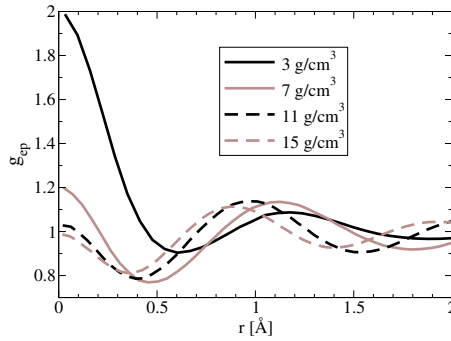
FIG. 9. (Color online) Electron-proton pair-correlation function in superionic water at 4000 K. The electrons delocalize at higher densities. The peaks at nonzero distance originate from the electron density which is located around oxygen ions neighboring the protons.

increases with the density. In liquid water under ambient conditions (density of 0.998 g/cm^3), an effective charge of $+0.52e$ for protons bound in H_2O molecules is computed which is in excellent agreement with the experimental values.[66,67] In ice X,[68,69] which is one of the ice phases that borders the superionic phase at lower temperatures, we determine an effective charge of $+e$ for a proton in a symmetric hydrogen bond which indicates that ice X (at a density of 4 g/cm^3) is an ionic crystal. The same value is obtained for the mobile protons in superionic water at an identical density and 3000 K.

However, the effective charges from linear-response polarization theory are not necessarily the same charges that are transported by protons along their entire trajectories. Using a Wannier representation of the electronic wave functions, it was shown that the positions of the nearest two Wannier centers (which mark electron pairs) remain largely unchanged when a proton is hopping to from one molecule to the next.[8,13,70] This leads one to the conclusion that the proton transports its unscreened charge of $+e$ when traveling typical intermolecular distances.

In this work, we rely on the results from the Wannier center analyses,[8,13,70] which are also partially concordant with those from polarization theory, and employ a proton charge of $+e$ for all considered densities and temperatures.

TABLE IV. Comparison of the estimated oxygen ionic conductivity with the protonic and electronic conductivity.

T (K)	ϱ (g/cm^3)	σ_O (1/Ω cm)	σ_p (1/Ω cm)	σ_e (1/Ω cm)
1000	1.75	0.2	1.9	
4000	2	7.7	62	47
8000	2	26	128	350

APPENDIX B: IONIC CONDUCTIVITY OF OXYGEN

As soon as molecular dissociation occurs, oxygen ions contribute to the conductivity as in a molten salt. With the relation

$$\sigma_O = \frac{(2e)^2 n_O}{k_B T} D_O (1 - \gamma), \tag{B1}$$

the oxygen conductivity can be estimated in a similar manner to the proton conductivity, see Eq. (1). In the above relation, n_O is the number of oxygen nuclei per volume and γ the fraction of protons bound to O^{2-} ions. It is the last factor in Eq. (B1) that suppresses the oxygen conductivity when water is largely molecular and in the limit of total dissociation ($\gamma = 0$) the expression is an Einstein formula.

In Table IV, some values of the oxygen conductivity are compared with the protonic and the electronic contribution. The oxygen conductivity increases with the protonic conductivity but never exceeds 10% of the total conductivity. Furthermore, the occurrence of twofold negatively charged oxygen ions is highly questionable when ionization takes place. Goldman et al.[9] have found in similar simulations that most of the occupied electronic states near the band gap are from negatively charged oxygen ions. Therefore, we expect these electrons to become conduction electrons first as the electronic conductivity rises. The oxygen ions will consequently carry a smaller negative charge than $2e$ which makes Eq. (B1) an upper limit for the oxygen conductivity. Since the oxygen conductivity values are not exceeding the uncertainty of the protonic and electronic conductivity, we refrain from precise calculations of the oxygen conductivity and neglect this contribution in our further discussions.

---

[1] D. Marx, ChemPhysChem **7**, 1848 (2006).
[2] W. B. Holzapfel, J. Chem. Phys. **50**, 4424 (1969).
[3] S. D. Hamann and M. Linton, Trans. Faraday Soc. **62**, 2234 (1966).
[4] A. C. Mitchell and W. J. Nellis, J. Chem. Phys. **76**, 6273 (1982).
[5] V. V. Yakushev, V. I. Postnov, V. E. Fortov, and T. I. Yakysheva, Sov. Phys. JETP **90**, 617 (2000).
[6] R. Chau, A. C. Mitchell, R. W. Minich, and W. J. Nellis, J. Chem. Phys. **114**, 1361 (2001).
[7] N. C. Holmes, W. J. Nellis, W. B. Graham, and G. E. Walrafen, Phys. Rev. Lett. **55**, 2433 (1985).
[8] E. Schwegler, G. Galli, F. Gygi, and R. Q. Hood, Phys. Rev.

Lett. **87**, 265501 (2001).
[9] N. Goldman, E. J. Reed, I.-F. W. Kuo, L. E. Fried, C. J. Mundy, and A. Curioni, J. Chem. Phys. **130**, 124517 (2009).
[10] M. French and R. Redmer, J. Phys.: Condens. Matter **21**, 375101 (2009).
[11] C. Cavazzoni, G. L. Chiarotti, S. Scandolo, E. Tosatti, M. Bernasconi, and M. Parrinello, Science **283**, 44 (1999).
[12] N. Goldman, L. E. Fried, I.-Feng W. Kuo, and C. J. Mundy, Phys. Rev. Lett. **94**, 217801 (2005).
[13] T. R. Mattsson and M. P. Desjarlais, Phys. Rev. Lett. **97**, 017801 (2006).
[14] E. Schwegler, M. Sharma, F. Gygi, and G. Galli, Proc. Natl.

Acad. Sci. U.S.A. **105**, 14779 (2008).

[15] M. French, T. R. Mattsson, N. Nettelmann, and R. Redmer, Phys. Rev. B **79**, 054107 (2009).

[16] B. Schwager, L. Chudinovskikh, A. Gavriliuk, and R. Boehler, J. Phys.: Condens. Matter **16**, S1177 (2004).

[17] A. F. Goncharov, N. Goldman, L. E. Fried, J. C. Crowhurst, I.-Feng W. Kuo, C. J. Mundy, and J. M. Zaug, Phys. Rev. Lett. **94**, 125508 (2005).

[18] J. F. Lin, E. Gregoryanz, V. V. Struzhkin, M. Somayazulu, H. K. Mao, and R. J. Hemley, Geophys. Res. Lett. **32**, L11306 (2005).

[19] B. Schwager and R. Boehler, High Press. Res. **28**, 431 (2008).

[20] A. F. Goncharov, C. Sanloup, N. Goldman, J. C. Crowhurst, S. Bastea, W. M. Howard, L. E. Fried, N. Guignot, M. Mezouar, and Y. Meng, J. Chem. Phys. **130**, 124514 (2009).

[21] P. M. Celliers, G. W. Collins, D. G. Hicks, M. Koenig, E. Henry, A. Benuzzi-Mounaix, D. Batani, D. K. Bradley, L. B. D. Silva, R. J. Wallace, S. J. Moon, J. H. Eggert, K. K. M. Lee, L. R. Benedetti, R. Jeanloz, I. M. N. Dague, B. Marchet, M. R. L. Gloahec, C. Reverdin, J. Pasley, O. Willi, D. Neely, and C. Danson, Phys. Plasmas **11**, L41 (2004).

[22] K. K. M. Lee, L. R. Benedetti, R. Jeanloz, P. M. Celliers, J. H. Eggert, D. G. Hicks, S. J. Moon, A. Mackinnon, L. B. D. Silva, D. K. Bradley, W. Unites, G. W. Collins, E. Henry, M. Koenig, A. Benuzzi-Mounaix, J. Pasley, and D. Neely, J. Chem. Phys. **125**, 014701 (2006).

[23] M. P. Desjarlais, Phys. Rev. B **68**, 064204 (2003).

[24] M. D. Knudson, M. P. Desjarlais, and D. H. Dolan, Science **322**, 1822 (2008).

[25] T. R. Mattsson, J. M. D. Lane, K. R. Cochrane, M. P. Desjarlais, A. P. Thompson, F. Pierce, and G. S. Grest, Phys. Rev. B **81**, 054103 (2010).

[26] A. R. Oganov, G. Price, and S. Scandolo, Z. Kristallogr. **220**, 531 (2005).

[27] M. J. Gillan, D. Alfe, J. Brodholt, L. Vocadlo, and G. D. Price, Rep. Prog. Phys. **69**, 2365 (2006).

[28] M. Podolak and R. T. Reynolds, Icarus **46**, 40 (1981).

[29] W. B. Hubbard, M. Podolak, and D. J. Stevenson, *Neptune and Triton* (University of Arizona Press, Tucson, AZ, 1995).

[30] M. Podolak, J. I. Podolak, and M. S. Marley, Planet. Space Sci. **48**, 143 (2000).

[31] N. Nettelmann, B. Holst, A. Kietzmann, M. French, R. Redmer, and D. Blaschke, Astrophys. J. **683**, 1217 (2008).

[32] J. J. Fortney and N. Nettelmann, Space Sci. Rev. **152**, 423 (2010).

[33] S. Stanley and J. Bloxham, Nature (London) **428**, 151 (2004).

[34] S. Stanley and J. Bloxham, Icarus **184**, 556 (2006).

[35] R. Redmer, T. R. Mattsson, N. Nettelmann, and M. French, Icarus (to be published).

[36] B. Holst, R. Redmer, and M. P. Desjarlais, Phys. Rev. B **77**, 184201 (2008).

[37] W. Lorenzen, B. Holst, and R. Redmer, Phys. Rev. Lett. **102**, 115701 (2009).

[38] N. Nettelmann, U. Kramm, R. Redmer, and R. Neuhäuser, Astron. Astrophys. (to be published).

[39] J. Heyd, G. E. Scuseria, and M. Ernzerhof, J. Chem. Phys. **118**, 8207 (2003).

[40] J. Heyd, G. E. Scuseria, and M. Ernzerhof, J. Chem. Phys. **124**, 219906 (2006).

[41] G. Kresse and J. Hafner, Phys. Rev. B **47**, 558 (1993).

[42] G. Kresse and J. Hafner, Phys. Rev. B **48**, 13115 (1993).

[43] G. Kresse and J. Hafner, Phys. Rev. B **49**, 14251 (1994).

[44] G. Kresse and J. Furthmüller, Phys. Rev. B **54**, 11169 (1996).

[45] J. Hafner, J. Comput. Chem. **29**, 2044 (2008).

[46] P. Hohenberg and W. Kohn, Phys. Rev. **136**, B864 (1964).

[47] W. Kohn and L. J. Sham, Phys. Rev. **140**, A1133 (1965).

[48] N. D. Mermin, Phys. Rev. **137**, A1441 (1965).

[49] P. E. Blöchl, Phys. Rev. B **50**, 17953 (1994).

[50] J. P. Perdew, K. Burke, and M. Ernzerhof, Phys. Rev. Lett. **77**, 3865 (1996).

[51] R. Kubo, J. Phys. Soc. Jpn. **12**, 570 (1957).

[52] D. A. Greenwood, Proc. Phys. Soc. London **71**, 585 (1958).

[53] J. Heyd, J. E. Peralta, G. E. Scuseria, and R. L. Martin, J. Chem. Phys. **123**, 174101 (2005).

[54] J. Paier, M. Marsman, K. Hummer, G. Kresse, I. C. Gerber, and J. G. Ángyán, J. Chem. Phys. **124**, 154709 (2006).

[55] T. S. Light, S. Licht, A. C. Bevilacqua, and K. R. Morash, Electrochem. Solid-State Lett. **8**, E16 (2005).

[56] S. Nosé, J. Chem. Phys. **81**, 511 (1984).

[57] The matrix elements are extracted out of the OPTIC file. It has to be ensured that all Bloch states are considered as initial and final.

[58] M. P. Desjarlais, J. D. Kress, and L. A. Collins, Phys. Rev. E **66**, 025401 (2002).

[59] A. Baldereschi, Phys. Rev. B **7**, 5212 (1973).

[60] H. J. Monkhorst and J. D. Pack, Phys. Rev. B **13**, 5188 (1976).

[61] J. Heyd and G. E. Scuseria, J. Chem. Phys. **121**, 1187 (2004).

[62] R. S. Mulliken, J. Chem. Phys. **23**, 1833 (1955).

[63] R. Resta, Ferroelectrics **136**, 51 (1992).

[64] R. D. King-Smith and D. Vanderbilt, Phys. Rev. B **47**, 1651 (1993).

[65] D. Vanderbilt and R. D. King-Smith, Phys. Rev. B **48**, 4442 (1993).

[66] Y. S. Badyal, M.-L. Saboungi, D. L. Price, S. D. Shastri, D. R. Haeffner, and A. K. Soper, J. Chem. Phys. **112**, 9206 (2000).

[67] J. Neuefeind, C. J. Benmore, B. Tomberli, and P. A. Egelstaff, J. Phys.: Condens. Matter **14**, L429 (2002).

[68] K. R. Hirsch and W. B. Holzapfel, Phys. Lett. A **101**, 142 (1984).

[69] A. Polian and M. Grimsditch, Phys. Rev. Lett. **52**, 1312 (1984).

[70] See supplementary material at http://link.aps.org/supplemental/10.1103/PhysRevLett.97.017801 for technical details concerning Ref. 13.